

Exploring the range of impacts of helium in the spectra of double detonation models for Type Ia supernovae

F. P. Callan,¹★ C. E. Collins,² S. A. Sim,¹ L. J. Shingles,² R. Pakmor,³ S. Srivastav,⁴ J. M. Pollin,¹ S. Gronow,⁵ F. K. Röpké^{5,6,7} and I. R. Seitenzahl⁵

¹*School of Mathematics and Physics, Queen’s University Belfast, University Road, Belfast BT7 1NN, UK*

²*GSI Helmholtzzentrum für Schwerionenforschung, Planckstraße 1, 64291 Darmstadt, Germany*

³*Max-Planck-Institut für Astrophysik, Karl-Schwarzschild-Str. 1, D-85748, Garching, Germany*

⁴*Astrophysics sub-Department, Department of Physics, University of Oxford, Keble Road, Oxford, OX1 3RH, UK*

⁵*Heidelberger Institut für Theoretische Studien, Schloss-Wolfsbrunnenweg 35, D-69118, Heidelberg, Germany*

⁶*Zentrum für Astronomie der Universität Heidelberg, Institut für Theoretische Astrophysik, Philosophenweg 12, D-69120 Heidelberg, Germany*

⁷*Zentrum für Astronomie der Universität Heidelberg, Astronomisches Rechen-Institut, Mönchhofstr. 12–14, 69120 Heidelberg, Germany*

Accepted XXX. Received YYY; in original form ZZZ

ABSTRACT

Models of sub-Chandrasekhar mass double detonations for Type Ia supernovae (SNe Ia) suggest a distinguishing property of this scenario is unburnt helium in the outer ejecta. However, modern explosion simulations suggest there may be significant variations in its mass and velocity distribution. We recently presented a NLTE (non local thermodynamic equilibrium) radiative transfer simulation for one realisation of the double detonation scenario with a modest He mass ($0.018 M_{\odot}$) present in the ejecta at relatively high velocities ($\sim 18000 \text{ km s}^{-1}$). That simulation predicted a He I 10830 Å feature blueward of Mg II 10927 Å consistent with near-infrared observations of “transitional” SNe Ia. To demonstrate the expected diversity in the helium signature, here we present a calculation for a double detonation model with a higher He mass ($\sim 0.04 M_{\odot}$) ejected at lower velocities ($\sim 13000 \text{ km s}^{-1}$). Despite our simulation predicting no clear optical or $2 \mu\text{m}$ helium features, a strong and persistent He I 10830 Å absorption is present. The feature appears at wavelengths consistent with the extended blue wing of the Mg II 10927 Å feature sometimes present in observations, suggesting this is a helium spectral signature (although for this particular model it is too strong and persistent to be consistent with normal SNe Ia). The significant differences in He I 10830 Å predicted by the two simulations suggests helium spectral signatures likely show significant variation throughout the SNe Ia population. This motivates further work to use this observable signature to test the parameter space for double detonation models.

Key words: radiative transfer – white dwarfs – supernovae: general – transients: supernovae – methods: numerical

1 INTRODUCTION

Type Ia supernovae (SNe Ia) are the thermonuclear explosions of at least one white dwarf (WD) in a close binary system. However, the nature of the progenitor systems and explosion mechanisms that produce SNe Ia are still uncertain. The *double detonation* is a widely discussed sub-Chandrasekhar (sub- M_{Ch}) explosion mechanism which has the potential to explain SNe Ia with a variety of luminosities. This scenario involves the ignition of a He detonation in a surface He layer (shell) on a carbon-oxygen (CO) WD (see, e.g., the study of He ignition by Glasner et al. 2018). The shock from the initial He detonation then results in the ignition of a secondary core detonation that entirely disrupts the WD. The mass of He required for a He detonation to occur depends on the specific explosion mechanism. For spontaneous ignition following stable mass transfer from a He star, massive He shells ($> 0.1 M_{\odot}$) are required (e.g. Nomoto 1980, 1982; Taam 1980; Livne 1990; Woosley & Weaver 1994; Hoefflich &

Khokhlov 1996; Nugent et al. 1997). This results in light curves and spectra incompatible with observations of normal SNe Ia due to the over-abundance of iron-group elements in the outer ejecta produced by the He detonation. If the stable mass transfer is instead from a degenerate companion, significantly less massive He shells are required ($< 0.1 M_{\odot}$ Bildsten et al. 2007; Shen & Bildsten 2009; Shen et al. 2010). We note that while it has been demonstrated that if such a He detonation occurs, a secondary core detonation will likely follow (Fink et al. 2010; Gronow et al. 2020, 2021; Boos et al. 2021), the initiation of the He detonation may be inhibited when rapid rotation is considered (see e.g. Neunteufel et al. 2017, 2019; Piersanti et al. 2024). In an alternative scenario, the He detonation may be triggered dynamically during the merger of two WDs (Shen & Moore 2014; Tanikawa et al. 2018, 2019; Pakmor et al. 2022; Shen et al. 2024), requiring only low He shell masses ($< 0.1 M_{\odot}$). Double detonation simulations invoking low He shell masses predict light curves and spectra that are much more consistent with normal SNe Ia (e.g. Kromer et al. 2010; Woosley & Kasen 2011; Polin et al. 2019; Shen

★ E-mail: f.callan@qub.ac.uk

et al. 2021a; Pollin et al. 2024; Collins et al. 2025 although see also Collins et al. 2022).

Noebauer et al. (2017) predict that the radioactive material produced in the outer layers of the ejecta from He shell burning in double detonation models can result in early light curve flashes. Additionally, simulations of double detonation models with more massive He shells ($\gtrsim 0.05 M_{\odot}$, e.g. Kromer et al. 2010; Sim et al. 2012; Polin et al. 2019; Collins et al. 2022) predict significant amounts of ultra-violet (UV) line blanketing due to the iron group elements synthesised in the He shell burning. A number of observed SNe Ia which exhibit either or both of these signatures have already been suggested as double detonation candidates (e.g. Inserra et al. 2015; Jiang et al. 2017; De et al. 2019; Jacobson-Galán et al. 2020; Dong et al. 2022; Ni et al. 2022; Liu et al. 2023; Padilla Gonzalez et al. 2023, 2024).

Another key characteristic of double detonation explosion models is that they predict significant masses of unburnt He in the ejecta ($\sim 0.01\text{--}0.1 M_{\odot}$, see e.g. Fink et al. 2010; Shen & Moore 2014; Gronow et al. 2020, 2021; Pakmor et al. 2022). Here we focus on the direct detection of this unburnt He as a signature of the double detonation scenario. The He ionization and excitation rates in supernova ejecta are strongly impacted by collisions with non-thermal electrons produced by γ rays from ^{56}Ni decays. NLTE (non local thermodynamic equilibrium) radiative transfer simulations that include a treatment for non-thermal processes are therefore required to predict if He spectral features are expected to form. As such, many previous radiative transfer simulations (e.g. Kromer et al. 2010; Woosley & Kasen 2011; Sim et al. 2012; Polin et al. 2019; Townsley et al. 2019; Gronow et al. 2020; Shen et al. 2021a; Collins et al. 2022; Pakmor et al. 2022; Pollin et al. 2024) have been unable to predict if He spectral features form.

The importance of collisions with non-thermal electrons for the formation of He features in type Ib/Ic supernovae has already been demonstrated (e.g. Chugai 1987; Lucy 1991; Hachinger et al. 2012). The formation of He I spectral features has also been investigated in previous radiative transfer simulations of SNe Ia models that include treatment for non-thermal electron collisions. Nugent et al. (1997) carried out a radiative transfer simulation for the thick He shell ($0.2 M_{\odot}$) double detonation model of Woosley & Weaver (1994) and reported no clear signatures of He in the model spectra, although the He I 10830 Å line did show substantial optical depths at some points in the model. Additionally, as part of their investigation of the prominent spectral absorption feature observed in the near-infrared (NIR) spectra of SN 1994D around 10500 Å, which Meikle et al. (1996) suggest could be either He I 10830 Å or Mg II 10927 Å, Mazzali & Lucy (1998) found that by introducing a few hundredths of a solar mass of He into the W7 deflagration model of Nomoto et al. (1984) a He I 10830 Å spectral feature could form. Dessart & Hillier (2015) also showed that He spectral features formed in their radiative transfer simulations of a He detonation model by Waldman et al. (2011). However, this model only considers a He detonation and produces light curves that are able to match only faint and fast declining events.

More recently Boyle et al. (2017) investigated whether He spectral features were expected to form for a double detonation model with a modest ejected He mass of $0.03 M_{\odot}$ (based on the explosion model of Fink et al. 2010). By using an analytical approximation to estimate the excited He I level populations they found He I 10830 Å and $2 \mu\text{m}$ lines may be formed by high velocity ($\sim 19000 \text{ km s}^{-1}$) He and the He I 10830 Å feature predicted may be consistent with a prominent absorption feature observed around 10300 Å in SN 2016dsg, an observed double detonation candidate (Dong et al. 2022). However, Boyle et al. (2017) utilised an approximate NLTE treatment that assumes the He II population is dominant. As it is not clear whether the

non-thermal ionization rate remains high enough to ensure He remains ionized, only an upper limit on the potential strength of the He features is possible with this approach. Therefore, radiative transfer simulations with a self-consistent calculation of the ionization state are required to investigate if He spectral features are expected for double detonation models that adopt more modest He shell masses. Collins et al. (2023) [hereafter C23] carried out such a simulation for the M2a double detonation model of Gronow et al. (2020) utilising a full NLTE treatment of the plasma conditions and also accounting for non-thermal electrons. This simulation showed a clear high velocity ($\sim 19000 \text{ km s}^{-1}$) He I 10830 Å feature that matches the evolution of a feature in the spectrum of the transitional SN Ia iPTF13ebh (Hsiao et al. 2015), demonstrating the potential of He spectral features as a signature of the double detonation scenario. However, due to blending with strong lines the exact contribution of He I to the optical spectra in the C23 model is not clear. Additionally, as a result of the limited signal to noise of the simulation, it was not possible to confirm whether the He $2 \mu\text{m}$ spectral feature, which could act as an independent confirmation of the presence of He, was expected to form in the model.

The amount of unburnt He, and its range of ejection velocity in the double detonation scenario can show significant variation for different lines of sight and between models (see e.g. figure 1 in Collins et al. 2022). Explosion simulations for models in which the He detonation is assumed to be ignited through compressional heating of accreted material predict very little unburnt He is present at velocities below $\sim 10000 \text{ km s}^{-1}$. In another widely discussed double-detonation scenario, the initial He shell detonation is instead ignited during the dynamical merger of two CO WDs which leads to a core detonation of the primary WD (Guillochon et al. 2010; Pakmor et al. 2013, 2022; Tanikawa et al. 2018, 2019; Boos et al. 2021, 2024; Shen et al. 2021b; Pollin et al. 2024). In this scenario the secondary WD may also explode via a double detonation (Tanikawa et al. 2019; Pakmor et al. 2022; Boos et al. 2024). Explosion simulations of such models predict unburnt He at generally lower velocities compared to accretion ignited double detonation models and for some lines of sight also show significant amounts of unburnt He at velocities below $\sim 10000 \text{ km s}^{-1}$ (see e.g. figure 1 of Pollin et al. 2024). The model presented by C23 is representative of a realisation of the double detonation scenario with He present at relatively high velocities (the He distribution peaks at $\sim 18000 \text{ km s}^{-1}$) and a reasonably large mass of ^{56}Ni present in the He shell detonation ash. In this paper, we instead investigate the potential of He spectral features to form for a realisation of the double detonation scenario with unburnt He present at significantly lower velocities (the He distribution peaks at $\sim 13000 \text{ km s}^{-1}$) and only a small mass of ^{56}Ni present in the He shell detonation ash. In particular, comparing the He spectral features predicted by our new model to those predicted by the model of C23 will provide insight into how sensitive the spectral signatures of He are to different model ejecta structures.

Throughout the study we compare the synthetic spectra produced to the normal SN 2011fe (Nugent et al. 2011) and the “transitional” SN 2022xkq (Pearson et al. 2024), which showed a similar feature around 10300 Å to the feature C23 identified as He I 10830 Å in the spectrum of SN iPTF13ebh. Note, the “transitional” SNe Ia we refer to throughout this work belong to subclass of fast declining SNe Ia described by Hsiao et al. (2015) that photometrically bridge the gap between subluminal 91bg-like and normal SNe Ia.

We describe our model ejecta structure and the radiative transfer simulation set up in Section 2. We then present our simulated spectra and comparisons with those of C23 as well as SN 2011fe and SN 2022xkq in Section 3 before presenting our conclusions in Section 4.

2 NUMERICAL METHODS

2.1 NLTE and non-thermal radiative transfer

The radiative transfer simulations are carried out using the time-dependent multi-dimensional Monte Carlo radiative transfer code ARTIS¹ (Sim 2007; Kromer & Sim 2009; Bulla et al. 2015; Shingles et al. 2020). ARTIS follows the methods of Lucy (2002, 2003, 2005) and is based on dividing the radiation field into indivisible energy packet Monte Carlo quanta. In this work (as in C23) we utilise the full NLTE and non-thermal capabilities added to ARTIS by Shingles et al. (2020). This includes a NLTE population and ionization solver and treatment for collisions with non-thermal leptons. To follow the energy distribution of high energy leptons which result from nuclear decays and Compton scattering of γ -rays, ARTIS solves the Spencer-Fano equation (as framed by Kozma & Fransson 1992). Auger electrons are allowed to contribute to heating, ionization and excitation. Excitation of bound electrons by non-thermal collisions is also included which was not the case for the simulation of C23.

For photoionization, following Lucy (2003), ARTIS utilises the full Monte Carlo photon-packet trajectories to obtain a rate estimator for each level pair while a parameterized radiation field is used to estimate transition rates for all other atomic processes. The atomic data set we use is based on the compilation of CMFGEN (Hillier 1990; Hillier & Miller 1998) and is similar to that described by Shingles et al. (2020) but with some additional ions. In this simulation we include He I-III, C I-IV, O I-IV, Ne I-III, Mg I-III, Si I-IV, S I-IV, Ar I-IV, Ca I-IV, Ti II-IV, Cr I-V, Fe I-V, Co II-V and Ni II-V.

The simulations also utilise the virtual packet scheme Bulla et al. (2015) implemented into ARTIS (which C23 did not utilise). Virtual packets significantly improve the signal to noise of the synthetic spectra produced with only a small computational penalty. Moreover, the virtual packet approach (see Bulla et al. 2015 for details) enables additional spectra to be extracted, in which the line opacity of specified atomic species are neglected, allowing their spectral contribution to be isolated. This is particularly useful for our investigation of potential NIR and optical He spectral features.

In previous work, C23 demonstrated that for the M2a double detonation model of Gronow et al. (2020) the spectral contribution of He is strongest in the first few days after explosion and then becomes weaker with time until it is no longer clearly contributing by two weeks after explosion. We therefore focus on relative early times in this work: the radiative transfer simulations are carried out between 1.5 and 35 d relative to explosion explosion, using 115 logarithmically spaced time steps. We adopt a grey approximation in optically thick cells (those with a Thomson optical depth greater than 1000). The initial time steps are treated in local thermodynamic equilibrium (LTE) and at time step 12 (2.1 d) the NLTE solver is switched on.

2.2 Double detonation ejecta model

The ejecta structure we simulate here is drawn from the 3D double detonation explosion model M08_03, described by Gronow et al. (2021). While ARTIS has the ability to carry out multi-dimensional simulations, utilising the full NLTE and non-thermal capabilities of ARTIS required to accurately assess whether He spectral features form is computationally expensive and has significant memory requirements owing to the large number of Monte Carlo estimators involved. Therefore, for this work we construct a 1D model from

the 3D M08_03 ejecta model. We note that the ejecta of SNe Ia explosion models are inherently multi-dimensional (e.g. Pakmor et al. 2024). In particular we note there are angular variations in the mass fractions of ⁵⁶Ni, He and the velocities at which material is ejected (see Collins et al. 2022 figure 1). These have significant impact as demonstrated by the approximate NLTE 3D radiative transfer simulation of the M08_03 model by Collins et al. (2022) that showed synthetic spectra with strong viewing angle dependencies. However, the 1D simulation presented here is an important initial investigation of the parameter space of potential He spectral signatures and will help identify which models may be of most interest to explore with multi-dimensional simulations in future work.

When constructing our 1D model we radially average cells in the 3D model that are contained within a solid angle cone centred on the negative z -axis to attempt to preserve the representative ejecta stratification and density profile of this radial direction in the 3D model. This is particularly important for investigating double detonation models because the velocity of the He shell ash varies noticeably with polar angle in the 3D double detonation models of Gronow et al. (2021) [see figure 1 in Collins et al. 2022]; thus if we impose spherical averaging we would effectively be artificially smoothing out the boundary region between the He shell ash and the core ejecta (in the 3D models, this boundary region is fairly sharply defined, but occurs at different velocities as a function of polar angle). We neglect the low density outer ejecta ($v > 26200 \text{ km s}^{-1}$) that become quickly optically thin and thus are not expected to contribute to the spectral formation for the times considered here. The ejecta composition of our model is shown in Figure 1.

The 1D ejecta model presented here has a total mass of $1.01 M_{\odot}$, a He mass of $0.04 M_{\odot}$ and a ⁵⁶Ni mass of $0.47 M_{\odot}$ whereas the original 3D ejecta model has a total mass of $0.83 M_{\odot}$, a He mass of $0.018 M_{\odot}$ and a ⁵⁶Ni mass of $0.13 M_{\odot}$. The greater He, ⁵⁶Ni and total mass of the 1D model are a result of significant asymmetries in the mass distribution of the 3D model with more mass ejected towards the negative z -axis (again see figure 1 in Collins et al. 2022). Thus, the 1D model constructed here is not a good representation of the original 3D model as a whole and will not preserve either its total energetics or luminosity. However, it does preserve the realistic radial structure from a representative double-detonation model, and has masses that are within the range expected for double detonation models (see e.g. table 3 in Fink et al. 2010). We note the greater mass of both ⁵⁶Ni and He in our model mean this model is likely representative of a line-of-sight exhibiting generally stronger He spectral features than the majority of the model viewing angles due to the increased number of non-thermal collisions with He expected.

The ejecta model simulated in this study is based on the negative z (south pole) region of the 3D M08_03 explosion model Gronow et al. (2020) presented (the He detonation is ignited on the positive z axis) while the C23 model is based on an equatorial slice of the 3D M2a explosion model presented by Gronow et al. (2020). As such the models show significant differences in their ejecta: although our model has a ⁵⁶Ni mass similar to the C23 ejecta model (0.47 and $0.49 M_{\odot}$ respectively) it has a total He mass ($0.04 M_{\odot}$) which is more than double that of the C23 model ($0.018 M_{\odot}$). Additionally, the ejecta structures show significant differences (compare Figure 1 and figure 1 in C23). In particular, for the C23 model the He lies at a relatively high velocity (peaking at $\sim 18000 \text{ km s}^{-1}$) and there is a significant mass of ⁵⁶Ni ($10^{-2} M_{\odot}$) present in the He shell. In contrast, the ejecta model investigated in this study shows a substantial mass of unburnt He at significantly lower velocities (peaking at $\sim 13000 \text{ km s}^{-1}$) with only a very small mass of ⁵⁶Ni ($< 10^{-4} M_{\odot}$) present in this region (such low ⁵⁶Ni to He ratios are characteristic of the negative z region

¹ <https://github.com/artis-mcrt/artis/>

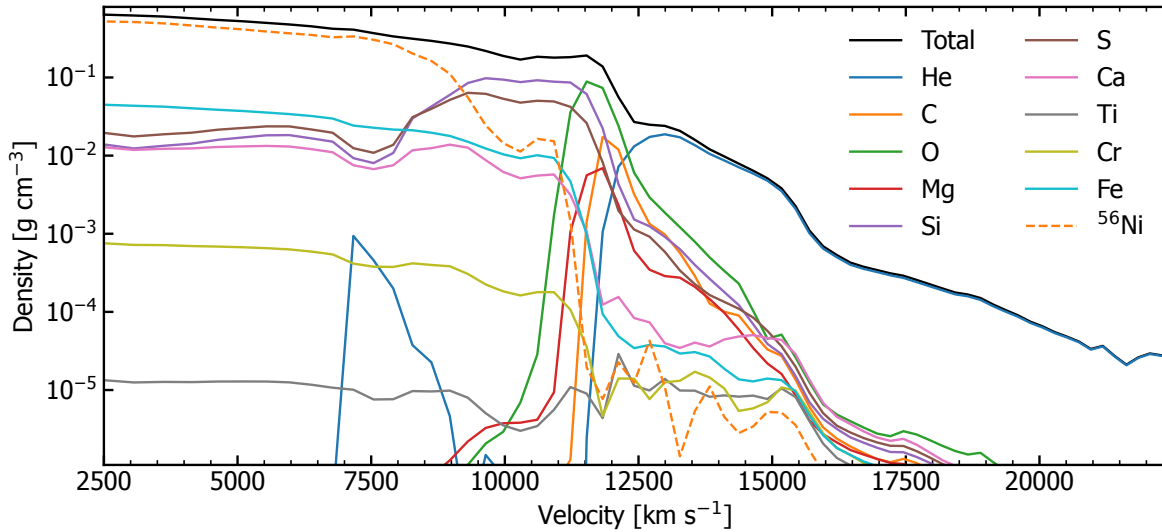


Figure 1. Model ejecta composition at 100 s after explosion.

in the [Gronow et al. \(2021\)](#) models, see [Collins et al. 2022](#) figure 1). As a result our new model has significantly less ^{56}Ni co-spatial with the unburnt He in the He shell relative to the C23 model. Therefore, the radiative transfer simulation presented here allows us to explore a significantly different realisation of the double detonation scenario than C23.

3 RESULTS

3.1 Helium spectral features

3.1.1 NIR He I 10830 Å

By far the strongest He spectral feature in our simulation is He I 10830 Å. Figure 2 shows the NIR spectroscopic evolution of our model around this feature (see also Figure A1). We also show the same calculation when the line opacity of He is omitted (as discussed in Section 2.1) to illustrate the impact on the spectrum of He absorption.

The model predicts a strong He I 10830 Å feature that persists for all epochs simulated. Although the profile shape changes with time the absorption is consistently around $\sim 12000 \text{ km s}^{-1}$. This is close to the velocity at which the density of unburnt He peaks (see Figure 1). The strength of this feature in our simulation confirms that He I 10830 Å can be an observable signature of the double detonation explosion scenario which provides a potentially powerful discriminant between double detonation models and other explosion scenarios which do not eject significant amounts of He.

3.1.2 Optical He I

Ideally, to confirm the presence of He in observations, we would like to identify a secondary He feature to corroborate the identification of He I 10830 Å. We therefore discuss the optical He features predicted by our simulation and the potential for them to be observed.

The He line that shows the strongest contribution to the optical spectra of our model (as quantified by the difference between the full spectra and the spectra lacking He line opacity) is He I 5876 Å. Some packets in the simulation do interact with the He I 5876 Å line for all

epochs shown in Figure 3, with the simulation predicting the number of interactions is greatest at early times and decreases with time. However, this does not result in a clear spectral feature forming in the model with the contribution of He I 5876 Å instead blending with the blue wing of the Si II 5972 Å feature. The next most prominent contribution of He to our model optical spectra is from He I 6678 Å. Again, while some packets are interacting with the He I 6678 Å line (until around *B*-peak) no clear spectral feature associated with this line is predicted by our model.

Thus, while this simulation predicts a strong and persistent He I 10830 Å feature, we do not find clear optical He features. This confirms that a lack of identifiable optical He features can not be used to rule out the presence of He, as previously demonstrated by the radiative transfer simulations of [Mazzali & Lucy \(1998\)](#) and C23. We also note [Nugent et al. \(1997\)](#) found no strong evidence for optical He in their radiative transfer simulation of a double detonation model.

3.1.3 NIR He I 2 μm

Since optical He features can not be used to corroborate the He I 10830 Å feature identification in observations, we now discuss the possibility of identifying a He I 2 μm feature in our simulation. Comparing the full model spectra to the model spectra in which He line opacity is neglected in Figure 2 (and Figure A1) we see that only a small number of packets in our simulation are interacting with the He I 2 μm line. We note that the spectral contribution of the He I 2 μm is greatest for the latest two epochs shown (5.1 and 10.3 d after *B*-peak), although it is still minor. Thus our simulation does not predict any clear He I 2 μm spectral feature is formed at any epochs considered here.

3.2 Comparisons to C23 and implications for He signature diversity

As discussed in Section 2.2 the model presented here represents a double detonation structure with a relatively substantial mass of ejected He ($0.04 M_{\odot}$), a significant fraction of He present at reasonably low velocities and only a small mass of ^{56}Ni present in the He shell detonation ash. In contrast the double detonation model

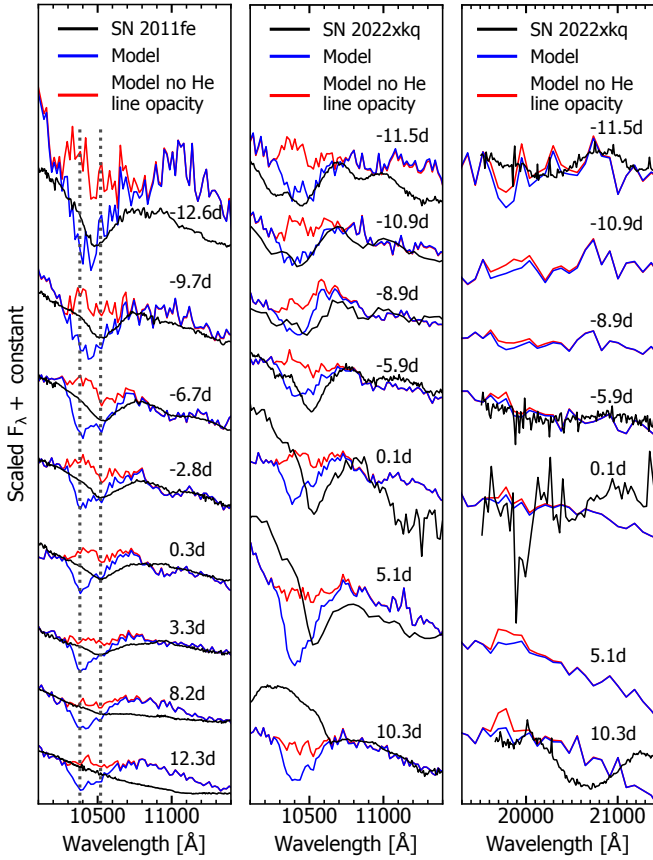


Figure 2. Evolution of model He I 10830 Å feature compared to SN 2011fe (Hsiao et al. 2013) and SN 2022xkq (Pearson et al. 2024). Also shown is the evolution of the He I 2 μm contribution predicted by the model compared to SN 2022xkq. In each case the full model spectra and the model spectra in which He line opacity is omitted are plotted. Times are relative to *B*-peak. The deepest absorption at 0.3 d for the simulated He I 10830 Å feature (left) and the Mg II 10927 Å feature observed for SN 2011fe (right) are indicated by the dotted lines for reference. Note, as the spectrum of SN 2022xkq is impacted by a telluric region redward of 2 μm this region of the spectrum of SN 2022xkq is not plotted in the right panel of the Figure for clarity.

presented by C23 has a significantly lower mass of ejected He ($0.018 M_{\odot}$), He present at higher velocities and a reasonably large mass of ^{56}Ni present in the He shell detonation ash. In the following we discuss the differences in the He features predicted by each of these models and comment on the implications of these differences for the double detonation scenario.

The He I 10830 Å feature predicted by our model forms at an approximately constant velocity ($\sim 12000 \text{ km s}^{-1}$) for all epochs simulated. The inner velocity of the He rich region in our model is at $\sim 11500 \text{ km s}^{-1}$ (see Figure 1). This suggests the spectral formation of He I 10830 Å is strongly influenced by material close to the inner boundary of the He shell. This is consistent with the structure of our model as the density of He peaks close to the inner boundary of the He shell at $\sim 13000 \text{ km s}^{-1}$ and the small mass of ^{56}Ni present in the He shell means the bulk of the non-thermal electrons that dominate the ionization of He likely originate from the ^{56}Ni rich inner regions of the ejecta. The spectral formation of the He I 10830 Å feature being dominated by this unburnt He in the inner regions of the He shell for all epochs also explains why the feature forms at constant velocity throughout the simulation.

In contrast, the He I 10830 Å feature predicted by the model of C23

appears at higher velocities and forms a separate feature to the blue wing of the Mg II 10927 Å feature (see C23 figure 3). The He feature in the C23 model also evolves to lower velocities with time: at 5 d after explosion the C23 feature is formed at $\sim 19500 \text{ km s}^{-1}$ but forms at $\sim 18000 \text{ km s}^{-1}$ at 2 weeks after explosion. The inner velocity of the region of unburnt He in the C23 model is at $\sim 15000 \text{ km s}^{-1}$ (see C23 figure 1) which suggests the C23 He feature does not depend so strongly on unburnt He close to the inner boundary of the He shell. This is consistent with the distribution of unburnt He in the C23 model which peaks at $\sim 18000 \text{ km s}^{-1}$ and shows a much more gradual drop off in density at higher velocities compared to the model presented in this study.

Neither our model nor the model of C23 predict any clear optical He I features. Additionally, while the C23 simulation did not have sufficient signal to noise to determine if a 2 μm feature appears, our simulation predicts no such feature forms, despite the much stronger and more persistent He I 10830 Å absorption relative to the C23 simulation. Together these models therefore suggest that He I 10830 Å is the most robust spectral signature of He and for double detonation models with moderate He shell masses (such as our model and the C23 model) other He I spectral lines (either optical or 2 μm) that can act as corroborating signatures will not necessarily appear. As such the absence of these He features should not be used to rule out the identification of He I 10830 Å.

Comparing the predictions of the two models also demonstrates that the spectral contribution of He I 10830 Å and its evolution with phase, strongly depends on the distribution of unburnt He in the model. Given that this can show substantial differences between models and with line-of-sight, we conclude that significant variation in the role of He I in shaping this feature is to be expected. This suggests there is substantial diversity in the observed He I 10830 Å spectral signature throughout the SN Ia population.

3.3 Spectral comparisons to observations

The double detonation scenario has been discussed as a potential explanation for both low luminosity SNe Ia, including members of the transitional sub-class, as well as normal luminosity SNe Ia. We therefore compare our model spectra to a representative normal luminosity SN Ia, SN 2011fe (Nugent et al. 2011; Pereira et al. 2013; Hsiao et al. 2013; Mazzali et al. 2014) and a representative transitional SN Ia, SN 2022xkq (Pearson et al. 2024). Both of these SNe have a large number of high quality early time NIR spectra and display prominent NIR spectral feature(s) at similar wavelengths to where the He I 10830 Å feature forms in our simulation. Therefore, comparisons between our model and the NIR features predicted by these SNe are of particular interest. To quantify if such comparisons are reasonable we first compare our model optical spectra to the optical spectra of SN 2011fe and SN 2022xkq.

3.3.1 Suitability of comparison objects

The model investigated in this work has a peak absolute *B*-band magnitude of -18.77 , which falls between that of SN 2011fe (-19.21 , Richmond & Smith 2012) and SN 2022xkq (-18.01 , Pearson et al. 2024). The luminosity match to each of these SNe is therefore sufficient that spectroscopic comparisons between our model and each of them is reasonable.

We first discuss the spectral comparison between our simulation and both SN 2011fe and SN 2022xkq in the optical, to assess how well the model can account for the observed spectral features. These comparisons are shown in Figure 4 where the different colours indicate

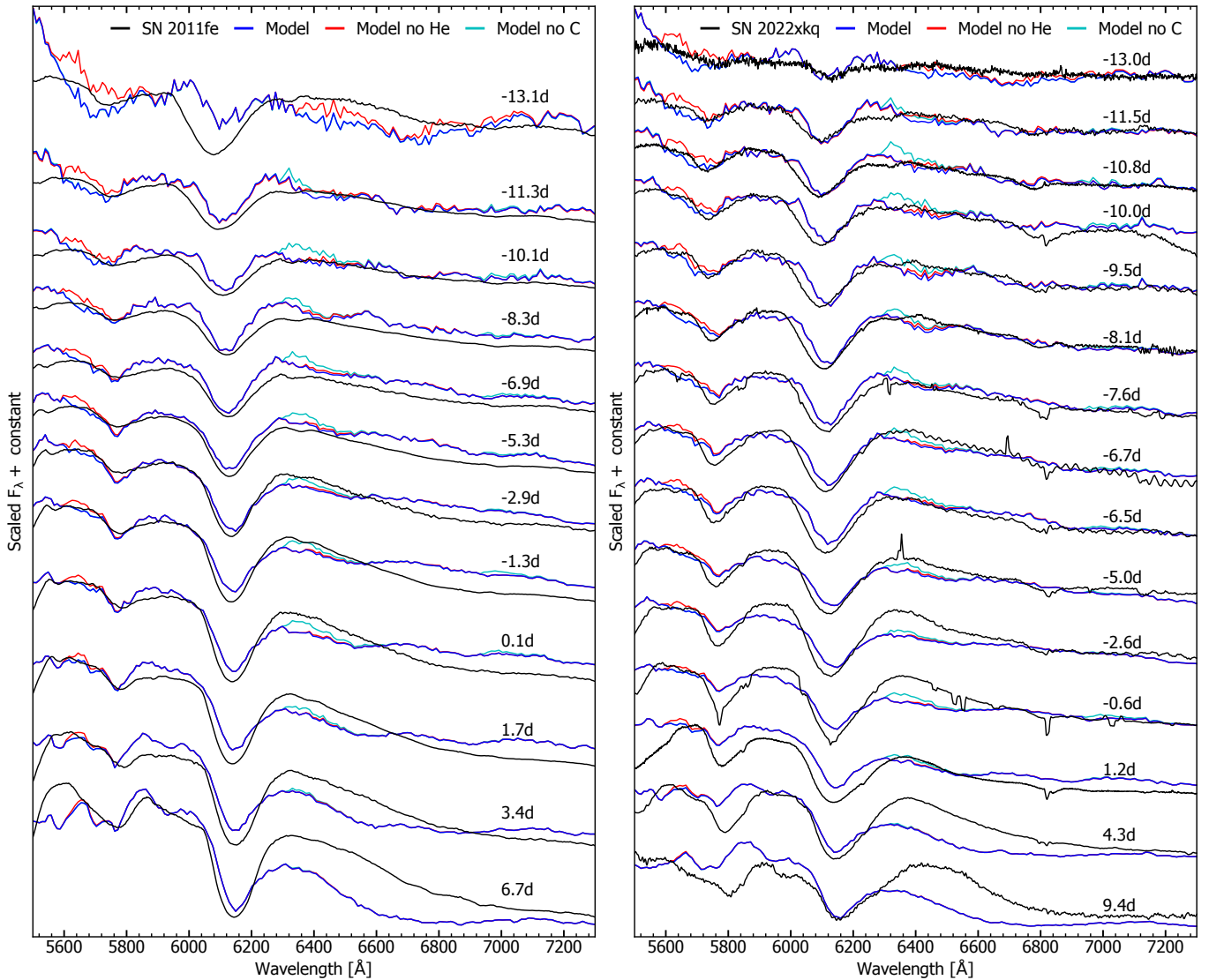


Figure 3. Model spectroscopic evolution of optical He I (5876 and 6678 Å) and C II (6580 and 7235 Å) lines compared to that of SN 2011fe (Pereira et al. 2013; Mazzali et al. 2014) and SN 2022xkq (Pearson et al. 2024). Also plotted are the model spectra in which the line opacities of He and C are not considered. Times are relative to *B*-peak.

the contributions of key species to the model spectra. From Figure 4 we see the spectral energy distribution (SED) predicted by our model provides a more successful match to the bluer SED exhibited by SN 2011fe (although the match to the SED of SN 2022xkq is still reasonable). This is primarily a result of both the model and SN 2011fe showing significantly less absorption blueward of ~ 4500 Å compared to SN 2022xkq. The model also provides a reasonable match to the strengths and velocities of a number of key features present in the spectra of both SNe, such as the prominent Si II λ 6355 and λ 5972 features, the Si II λ 5468 “W”, the Ca II NIR triplet and the O I λ 7773 feature. However, from peak onwards, some features in the spectra of SN 2022xkq redward of ~ 5000 Å are noticeably stronger than those predicted by the model. In particular the Si II λ 5972, O I λ 7773 and the Ca II NIR triplet are significantly stronger. The Si II λ 6355 feature does however show a relatively similar strength for the model and SN 2022xkq after peak (although the observed feature is a little too strong). We note that while the model provides a reasonable match to the Ca II H&K in both SNe, it is generally less successful at reproducing the spectral features exhibited by both

SN blueward of ~ 5000 Å. Overall, our model produces slightly better optical spectroscopic agreement with SN 2011fe over the epochs compared. However, the agreement of the model with both SNe is sufficient to justify the detailed comparisons of individual He spectral features, which are the primary focus of this study.

3.3.2 Simulated He I 10830 Å feature compared to observations

As discussed in Section 3.1.1, our simulation shows a strong feature due to He I 10830 Å. We now discuss how this feature compares to observations of the normal SN 2011fe and the transitional SN 2022xkq.

Figure 2 shows the NIR spectroscopic evolution of our model He features compared to SN 2011fe and SN 2022xkq. The full NIR spectroscopic evolution of the model compared to these SNe is shown in Figure A1. In Figures 2 and A1 the spectra have been scaled so features can be more easily compared.

First comparing to SN 2011fe (left panel Figure 2), we see the He

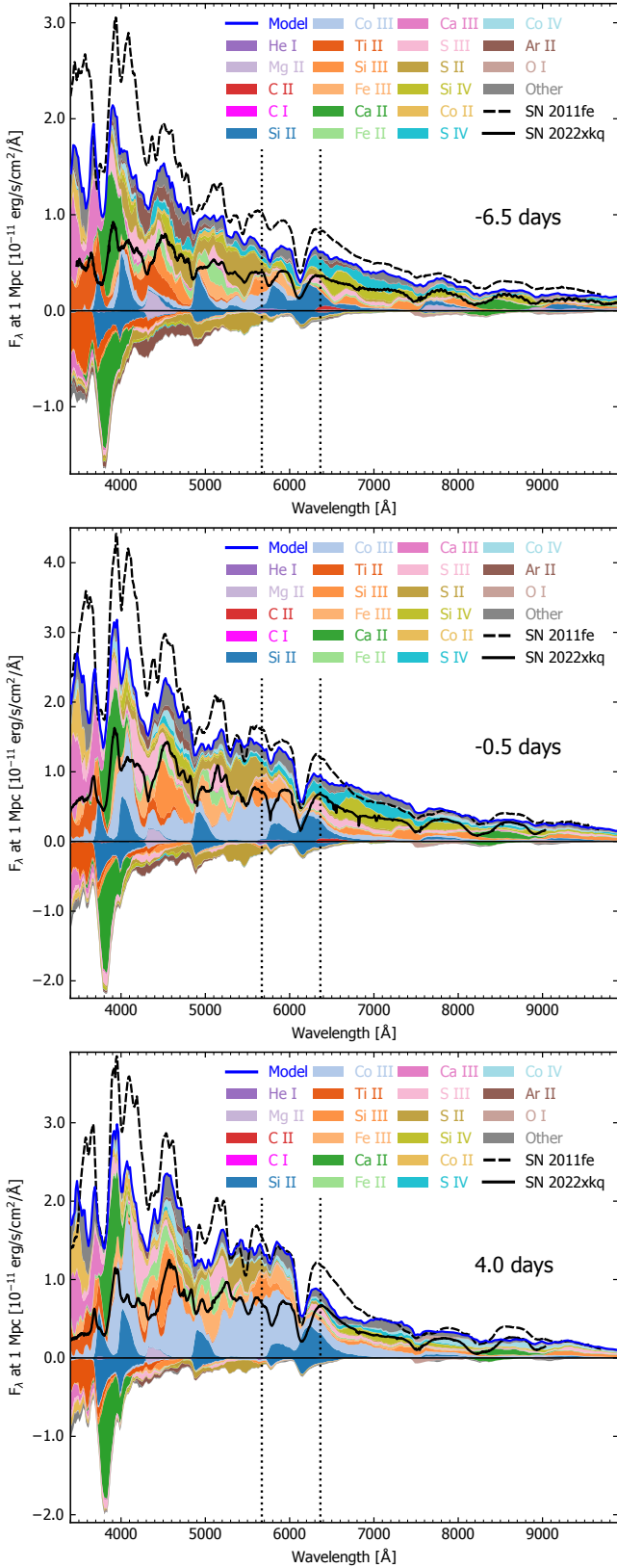


Figure 4. Absolute flux optical spectral comparisons between the model, with the contributions of key species indicated, SN 2011fe (Pereira et al. 2013) and SN 2022xkq (Pearson et al. 2024). For reference the dotted lines indicate the wavelengths of He I 5876 Å and C II 6580 Å absorption. Times are relative to *B*-peak.

feature predicted by our simulation overlaps with the feature Hsiao et al. (2013) identify as Mg II 10927 Å in SN 2011fe. In the spectra of SN 2011fe this feature shows an extended blue wing which Hsiao et al. (2013) attribute to C I 10693 Å (Marion et al. 2015 propose the same identification for SN 2014J, another normal SN Ia). However, our model does not predict any clear feature from C I 10693 Å (see Section 3.3.5 for further discussion). The strongest absorption of the model He feature is to the blue wing of the Mg feature in SN 2011fe. We therefore suggest this extended wing may instead be an observational signature of He I 10830 Å. In this interpretation the observed absorption feature forms from a strong blend of Mg II 10927 Å and He I 10830 Å with He I 10830 Å primarily contributing to the blue wing of the feature. We do however note the He feature predicted by our model (which represents a realisation of the double detonation scenario with a fairly substantial ejected He mass) is significantly too strong to be consistent with SN 2011fe (or SN 2014J). Therefore, further simulations for models with somewhat lower ejected He masses than the model presented here are desirable to investigate if they predict a He contribution to the blue wing of the Mg feature consistent with observations. We also note Mg II 10927 Å contributes to our model spectrum at wavelengths consistent with the Mg feature observed in the spectrum of SN 2011fe. However the contribution of Mg II 10927 Å is weaker than that of He I 10830 Å in our simulation for all epochs simulated.

Now focusing on comparisons with SN 2022xkq (middle panel of Figure 2), we see SN 2022xkq also shows a strong absorption feature that Pearson et al. (2024) identify as Mg II 10927 Å. The He I 10830 Å feature predicted by our model again overlaps with this Mg II feature.

However, SN 2022xkq also shows a weaker secondary absorption feature to the blue of the Mg feature that disappears by peak (this feature is also observed at early times in other transitional SNe Ia, see e.g. Hsiao et al. 2015; Wyatt et al. 2021). Our model does not predict any such double absorption feature and the He I 10830 Å feature predicted by our model forms at too low a velocity to match the secondary absorption feature. However, as discussed in Section 3.2 the double detonation model of C23 does predict such a double feature with Mg II 10927 Å forming the primary absorption feature and high velocity He I 10830 Å forming the secondary feature. C23 demonstrated this simulated feature was consistent with the double absorption feature observed in the spectrum of another transitional SN, iPTF13ebh (Hsiao et al. 2015) which is very similar to the feature observed in the spectrum of SN 2022xkq. We note that previous studies have suggested this secondary absorption feature observed in the spectra of some SNe Ia is instead formed by C I 10693 Å (e.g. Höflich et al. 2002; Hsiao et al. 2015; Wyatt et al. 2021; Li et al. 2022; Pearson et al. 2024), however neither our model nor the C23 model show any such C I 10693 Å spectral feature (see Section 3.3.5 for further discussion).

3.3.3 Optical He spectral contribution and observations

The simulation showed no clearly identifiable He features in the optical (as was the case for the model of C23), but nonetheless we now discuss how the optical regions with slight He contributions compare with the observations.

From Figure 3 we can see that compared to SN 2011fe and SN 2022xkq the blue wing of the Si II 5972 Å feature in our full model spectra predicts generally too much absorption while the model spectra in which line opacity from He is excluded does not predict enough absorption. As such, for all epochs compared, both sets of model

spectra provide a similar match to the blue wing of the observed Si II 5972 Å feature.

The next strongest expected He line is He I 6678 Å. The very weak spectral contribution from He I 6678 Å in the simulation does not impact the agreement with either SN 2011fe or SN 2022xkq over the wavelength range to which it contributes. Therefore, the presence of strong He I 10830 Å, as is the case for the double detonation model we present here, does not require that there are strong, clearly observable optical He features.

3.3.4 He I 2 μm feature and observations

A clear He I 2 μm feature is not predicted by this simulation. The 0.04 M_⊙ of He ejected by the model we investigate here is likely towards the upper limit of the ejected He mass that can be present in a model for it to still produce reasonable agreement with the optical spectra of normal and transitional SNe Ia (Kromer et al. 2010). The weak contribution of He I 2 μm in our simulation (see Figure 2) therefore suggests it is very unlikely that such a feature would be observable for any normal or transitional SNe Ia. This is consistent with the fact that neither SN 2011fe or SN 2022xkq show any spectral feature around 2 μm. Therefore, the presence of strong He I 10830 Å does not require that a 2 μm feature is also observed. We note however that even if this feature can form, observing it will be challenging for ground based telescopes because the spectral contribution of the He I 2 μm line predicted by the model lies very close to a telluric region (see right panel in Figure 2) and thus the observed spectra are likely still impacted by the proximity to this region. For example, the observed SN 2022xkq spectrum at 0.1 d after B-peak shows what appears to be an absorption feature around 2 μm. However, the potential feature does not show a consistent evolution in the observed spectra and only appears for a single epoch and thus is very unlikely to be a real feature (Pearson et al. 2024). Therefore space based (e.g. JWST) observations will likely be required to observe any potential 2 μm feature.

3.3.5 Spectral contribution of C and observations

C I 10693 Å has been proposed to have an observable contribution to the blue wing of the Mg II 10927 Å feature in SNe Ia before peak, either as an extended blue wing (e.g. Hsiao et al. 2013; Marion et al. 2015) or a distinct secondary feature (e.g. Höflich et al. 2002; Hsiao et al. 2015; Wyatt et al. 2021; Li et al. 2022; Pearson et al. 2024). We therefore comment here on the spectral contribution of C in our simulation and the C23 simulation.

Neither our model or the C23 model predicts any clear feature from C I 10693 Å. This is not unexpected as the ion population of C II dominates over that of C I for both simulations. This is consistent with the findings of previous studies (e.g. Tanaka et al. 2008; Heringer et al. 2019) although we do note that some simulations have shown C I features can form for different classes of explosion models (e.g. Höflich et al. 2002; Blondin et al. 2013, 2017; Hsiao et al. 2015).

Our model does show some contribution from C II in the optical. In particular, a weak C II 6580 Å feature forms on the red shoulder of the Si II 6355 Å feature from ~7 d before up until B-peak. This feature appears at a velocity generally consistent with the C II 6580 Å feature observed in the spectra of SN 2011fe and SN 2022xkq. We also see a weak spectral contribution from C II 7235 Å (again see Figure 3), however the contribution is so weak that it never produces any clear spectral feature. We note that while the C23 simulation also shows

contributions from C II 6580 and 7235 Å, unlike our simulation no clear C II 6580 Å feature forms due to blending with stronger lines.

The amount of C ejected can vary significantly between different double detonation models. For example, the 3D double detonation model sequence of Gronow et al. (2021) shows a variation in C mass between models of 2.8×10^{-5} to $1.5 \times 10^{-2} M_{\odot}$. The model we present here has an ejected C mass of $9 \times 10^{-3} M_{\odot}$. While this is representative of a relatively carbon rich representation of the double detonation scenario it is still well within the range of ejected C masses predicted for double detonation models. As such the clear C II 6580 Å feature this model predicts demonstrates that the presence of optical C II can not be used to rule out the double detonation scenario.

4 CONCLUSIONS

We have carried out a NLTE radiative transfer simulation including treatment for non-thermal electrons for a realisation of the double detonation scenario with a modest mass of He (0.04 M_⊙) that is ejected from the outer helium layer with relatively low velocities (~13000 km s⁻¹). The model is representative of the negative polar direction in the 3D Gronow et al. (2021) model on which it is based (where the He detonation is ignited in the positive polar direction). We find our model predicts a strong and persistent He I 10830 Å spectral feature that is strongly blended with the spectral contribution of Mg II 10927 Å. This Mg II feature shows an extended wing in the spectra of some normal SNe Ia that has previously been attributed to C I 10693 Å (Hsiao et al. 2013; Marion et al. 2015). However, the He I 10830 Å feature predicted by our simulation has its strongest absorption to the blue wing of this Mg II 10927 Å feature and our model does not predict a C I 10693 Å feature forms. We therefore suggest the extended wing may instead be a spectral signature of He, although we note the He feature predicted by our particular model is too strong and persistent to be consistent with normal SNe Ia.

Despite the strong He I 10830 Å feature predicted by our simulation no clear optical He spectral features appear. Therefore, consistent with what C23 found for their double detonation simulation, our simulation demonstrates that the non-detection of optical He features can not be used to rule out the He I 10830 Å spectral feature. Our simulation also predicted no clear He I 2 μm feature forms, demonstrating the absence of He I 2 μm also does not rule out He I 10830 Å (the C23 simulation did not have sufficient signal to noise to test the formation of the He I 2 μm feature). The He mass of our model is likely towards the high end of what can be ejected while still producing reasonable agreement with the optical spectra of normal and transitional SNe Ia (Kromer et al. 2010) which suggests observed He I 10830 Å spectral signatures present in the spectra of normal or transitional SNe Ia are not necessarily accompanied by additional He signatures.

Relative to our simulation, the double detonation model presented by C23 (which also included a full treatment of NLTE and non-thermal processes) has a significantly lower He ejecta mass (0.018 M_⊙), present at higher velocities (~18000 km s⁻¹) and is representative of the equatorial direction in the 3D Gronow et al. (2020) model on which it is based. The contribution of He I 10830 Å is weaker and present at higher velocities for the C23 simulation, forming a distinct feature blueward of Mg II 10927 Å which is no longer clearly present by peak. This feature is consistent with a feature present in the pre-peak spectra of observed transitional SNe Ia (Hsiao et al. 2015; Wyatt et al. 2021; Pearson et al. 2024). Together these simulations demonstrate that the He signatures predicted by double detonation models can show substantial variation depend-

ing on the exact realisation of the ejecta structure, and in particular the distribution of unburnt He, which is both model and line-of-sight dependent. This implies significant diversity is expected in the He I 10830 Å spectral signature across the observed SN Ia population. This should be tested with observations of the pre-peak NIR spectroscopic evolution for a larger sample of SNe Ia.

Future work should also focus on full NLTE multi-dimensional radiative transfer simulations of double detonation models that will allow the viewing angle variation of predicted He spectral signatures to be explored. In particular, since both our simulation and the C23 simulation predict a He I 10830 Å spectral signature too strong compared to normal SNe Ia, double detonation models with lower masses of ejected He should be prioritised. Such simulations will be key to determining whether realisations of the double detonation scenario exist that predict He spectral signatures consistent with the NIR spectra of normal SNe Ia and will also allow us to probe the lower limit of He that can be ejected while still producing an observable signature.

ACKNOWLEDGEMENTS

FPC and SAS, acknowledge funding from STFC grant ST/X00094X/1. This work used the DiRAC Memory Intensive service (Cosma8) at Durham University, managed by the Institute for Computational Cosmology on behalf of the STFC DiRAC HPC Facility (www.dirac.ac.uk). The DiRAC service at Durham was funded by BEIS, UKRI and STFC capital funding, Durham University and STFC operations grants. Access to DiRAC resources was granted through a Director's Discretionary Time allocation in 2023/24. This work also used the DiRAC Data Intensive service (CSD3) at the University of Cambridge, managed by the University of Cambridge University Information Services on behalf of the STFC DiRAC HPC Facility (www.dirac.ac.uk). The DiRAC component of CSD3 at Cambridge was funded by BEIS, UKRI and STFC capital funding and STFC operations grants. DiRAC is part of the UKRI Digital Research Infrastructure. The authors gratefully acknowledge the Gauss Centre for Supercomputing e.V. (www.gauss-centre.eu) for funding this project by providing computing time on the GCS Supercomputer JUWELS at Jülich Supercomputing Centre (JSC). CEC acknowledges funding by the European Union (ERC, HEAVYMETAL, 101071865). LJS acknowledges support by the European Research Council (ERC) under the European Union's Horizon 2020 research and innovation program (ERC Advanced Grant KILONOVA No. 885281). LJS acknowledges support by Deutsche Forschungsgemeinschaft (DFG, German Research Foundation) - Project-ID 279384907 - SFB 1245 and MA 4248/3-1. JMP acknowledges the support of the Department for Economy (DFE). The work of FKR is supported by the European Union (ERC, ExCEED, 101096243) and by the Deutsche Forschungsgemeinschaft (DFG, German Research Foundation) - project number 537700965. Views and opinions expressed are however those of the author(s) only and do not necessarily reflect those of the European Union or the European Research Council. Neither the European Union nor the granting authority can be held responsible for them. This work was supported in part by the European Union (ChETEC-INFRA, project no. 101008324), NSF/IRENA and the Klaus Tschira Foundation. NumPy and SciPy (Oliphant 2007), Matplotlib (Hunter 2007) and ARTISTOOLS² (Shingles et al. 2025) were used for data processing and plotting.

DATA AVAILABILITY

The spectra presented here will be made available on the Heidelberg supernova model archive HESMA³ (Kromer et al. 2017).

REFERENCES

- Bildsten L., Shen K. J., Weinberg N. N., Nelemans G., 2007, *ApJ*, **662**, L95
 Blondin S., Dessart L., Hillier D. J., Khokhlov A. M., 2013, *MNRAS*, **429**, 2127
 Blondin S., Dessart L., Hillier D. J., Khokhlov A. M., 2017, *MNRAS*, **470**, 157
 Boos S. J., Townsley D. M., Shen K. J., Caldwell S., Miles B. J., 2021, *ApJ*, **919**, 126
 Boos S. J., Townsley D. M., Shen K. J., 2024, *ApJ*, **972**, 200
 Boyle A., Sim S. A., Hachinger S., Kerzendorf W., 2017, *A&A*, **599**, A46
 Bulla M., Sim S. A., Kromer M., 2015, *MNRAS*, **450**, 967
 Chugai N. N., 1987, *Soviet Astronomy Letters*, **13**, 282
 Collins C. E., Gronow S., Sim S. A., Röpke F. K., 2022, *MNRAS*, **517**, 5289
 Collins C. E., Sim S. A., Shingles L. J., Gronow S., Röpke F. K., Pakmor R., Seitenzahl I. R., Kromer M., 2023, *MNRAS*, **524**, 4447
 Collins C. E., et al., 2025, *MNRAS*, **538**, 1289
 De K., et al., 2019, *ApJ*, **873**, L18
 Dessart L., Hillier D. J., 2015, *MNRAS*, **447**, 1370
 Dong Y., et al., 2022, *ApJ*, **934**, 102
 Fink M., Röpke F. K., Hillebrandt W., Seitenzahl I. R., Sim S. A., Kromer M., 2010, *A&A*, **514**, A53
 Glasner S. A., Livne E., Steinberg E., Yalinewich A., Truran J. W., 2018, *Monthly Notices of the Royal Astronomical Society*, **476**, 2238
 Gronow S., Collins C., Ohlmann S. T., Pakmor R., Kromer M., Seitenzahl I. R., Sim S. A., Röpke F. K., 2020, *A&A*, **635**, A169
 Gronow S., Collins C. E., Sim S. A., Röpke F. K., 2021, *A&A*, **649**, A155
 Guillochon J., Dan M., Ramirez-Ruiz E., Rosswog S., 2010, *ApJ*, **709**, L64
 Hachinger S., Mazzali P. A., Taubenberger S., Hillebrandt W., Nomoto K., Sauer D. N., 2012, *MNRAS*, **422**, 70
 Heringer E., van Kerkwijk M. H., Sim S. A., Kerzendorf W. E., Graham M. L., 2019, *ApJ*, **871**, 250
 Hillier D. J., 1990, *A&A*, **231**, 116
 Hillier D. J., Miller D. L., 1998, *ApJ*, **496**, 407
 Hoefflich P., Khokhlov A., 1996, *ApJ*, **457**, 500
 Höflich P., Gerardy C. L., Fesen R. A., Sakai S., 2002, *ApJ*, **568**, 791
 Hsiao E. Y., et al., 2013, *ApJ*, **766**, 72
 Hsiao E. Y., et al., 2015, *A&A*, **578**, A9
 Hunter J. D., 2007, *Computing in Science and Engineering*, **9**, 90
 Inserra C., et al., 2015, *ApJ*, **799**, L2
 Jacobson-Galán W. V., et al., 2020, *ApJ*, **896**, 165
 Jiang J.-A., et al., 2017, *Nature*, **550**, 80
 Kozma C., Fransson C., 1992, *ApJ*, **390**, 602
 Kromer M., Sim S. A., 2009, *MNRAS*, **398**, 1809
 Kromer M., Sim S. A., Fink M., Röpke F. K., Seitenzahl I. R., Hillebrandt W., 2010, *ApJ*, **719**, 1067
 Kromer M., Ohlmann S., Röpke F. K., 2017, *Mem. Soc. Astron. Italiana*, **88**, 312
 Li Z., et al., 2022, *ApJ*, **927**, 142
 Liu C., et al., 2023, *ApJ*, **958**, 178
 Livne E., 1990, *ApJ*, **354**, L53
 Lucy L. B., 1991, *ApJ*, **383**, 308
 Lucy L. B., 2002, *A&A*, **384**, 725
 Lucy L. B., 2003, *A&A*, **403**, 261
 Lucy L. B., 2005, *A&A*, **429**, 19
 Marion G. H., et al., 2015, *ApJ*, **798**, 39
 Mazzali P. A., Lucy L. B., 1998, *MNRAS*, **295**, 428
 Mazzali P. A., et al., 2014, *MNRAS*, **439**, 1959
 Meikle W. P. S., et al., 1996, *MNRAS*, **281**, 263

² <https://github.com/artis-mcrt/artistools>

³ <https://hesma.h-its.org>

- Neunteufel P., Yoon S. C., Langer N., 2017, *A&A*, **602**, A55
- Neunteufel P., Yoon S. C., Langer N., 2019, *A&A*, **627**, A14
- Ni Y. Q., et al., 2022, *Nature Astronomy*, **6**, 568
- Noebauer U. M., Kromer M., Taubenberger S., Baklanov P., Blinnikov S., Sorokina E., Hillebrandt W., 2017, *MNRAS*, **472**, 2787
- Nomoto K., 1980, *Space Science Reviews*, **27**, 563
- Nomoto K., 1982, *ApJ*, **253**, 798
- Nomoto K., Thielemann F. K., Wheeler J. C., 1984, *ApJ*, **279**, L23
- Nugent P., Baron E., Branch D., Fisher A., Hauschildt P. H., 1997, *ApJ*, **485**, 812
- Nugent P. E., et al., 2011, *Nature*, **480**, 344
- Oliphant T. E., 2007, *Computing in Science & Engineering*, **9**, 10
- Padilla Gonzalez E., et al., 2023, *ApJ*, **953**, 25
- Padilla Gonzalez E., et al., 2024, *ApJ*, **964**, 196
- Pakmor R., Kromer M., Taubenberger S., Springel V., 2013, *ApJ*, **770**, L8
- Pakmor R., et al., 2022, *MNRAS*, **517**, 5260
- Pakmor R., Seitenzahl I. R., Ruiter A. J., Sim S. A., Röpke F. K., Taubenberger S., Bieri R., Blondin S., 2024, *A&A*, **686**, A227
- Pearson J., et al., 2024, *ApJ*, **960**, 29
- Pereira R., et al., 2013, *A&A*, **554**, A27
- Piersanti L., Yungelson L. R., Bravo E., 2024, *A&A*, **689**, A287
- Polin A., Nugent P., Kasen D., 2019, *ApJ*, **873**, 84
- Pollin J. M., Sim S. A., Pakmor R., Callan F. P., Collins C. E., Shingles L. J., Röpke F. K., Srivastav S., 2024, *MNRAS*, **533**, 3036
- Richmond M. W., Smith H. A., 2012, *JAASO*, **40**, 872
- Shen K. J., Bildsten L., 2009, *ApJ*, **699**, 1365
- Shen K. J., Moore K., 2014, *ApJ*, **797**, 46
- Shen K. J., Kasen D., Weinberg N. N., Bildsten L., Scannapieco E., 2010, *ApJ*, **715**, 767
- Shen K. J., Blondin S., Kasen D., Dessart L., Townsley D. M., Boos S., Hillier D. J., 2021a, *ApJ*, **909**, L18
- Shen K. J., Boos S. J., Townsley D. M., Kasen D., 2021b, *ApJ*, **922**, 68
- Shen K. J., Boos S. J., Townsley D. M., 2024, *ApJ*, **975**, 127
- Shingles L. J., et al., 2020, *MNRAS*, **492**, 2029
- Shingles L. J., Collins C. E., Holas A., Callan F., Sim S., 2025, *artistools*, doi:10.5281/zenodo.7728326, <https://github.com/artis-mcrt/artistools>
- Sim S. A., 2007, *MNRAS*, **375**, 154
- Sim S. A., Fink M., Kromer M., Röpke F. K., Ruiter A. J., Hillebrandt W., 2012, *MNRAS*, **420**, 3003
- Taam R. E., 1980, *ApJ*, **242**, 749
- Tanaka M., et al., 2008, *ApJ*, **677**, 448
- Tanikawa A., Nomoto K., Nakasato N., 2018, *ApJ*, **868**, 90
- Tanikawa A., Nomoto K., Nakasato N., Maeda K., 2019, *ApJ*, **885**, 103
- Townsley D. M., Miles B. J., Shen K. J., Kasen D., 2019, *ApJ*, **878**, L38
- Waldman R., Sauer D., Livne E., Perets H., Glasner A., Mazzali P., Truran J. W., Gal-Yam A., 2011, *ApJ*, **738**, 21
- Woosley S. E., Kasen D., 2011, *ApJ*, **734**, 38
- Woosley S. E., Weaver T. A., 1994, *ApJ*, **423**, 371
- Wyatt S. D., et al., 2021, *ApJ*, **914**, 57

APPENDIX A: NIR SPECTRAL EVOLUTION

In Figure A1 we show the NIR spectra for our full model and a model in which the line opacity of He is omitted. These are compared to observations of SN 2011fe (Hsiao et al. 2013) and SN 2022xkq (Pearson et al. 2024).

This paper has been typeset from a $\text{\TeX}/\text{\LaTeX}$ file prepared by the author.

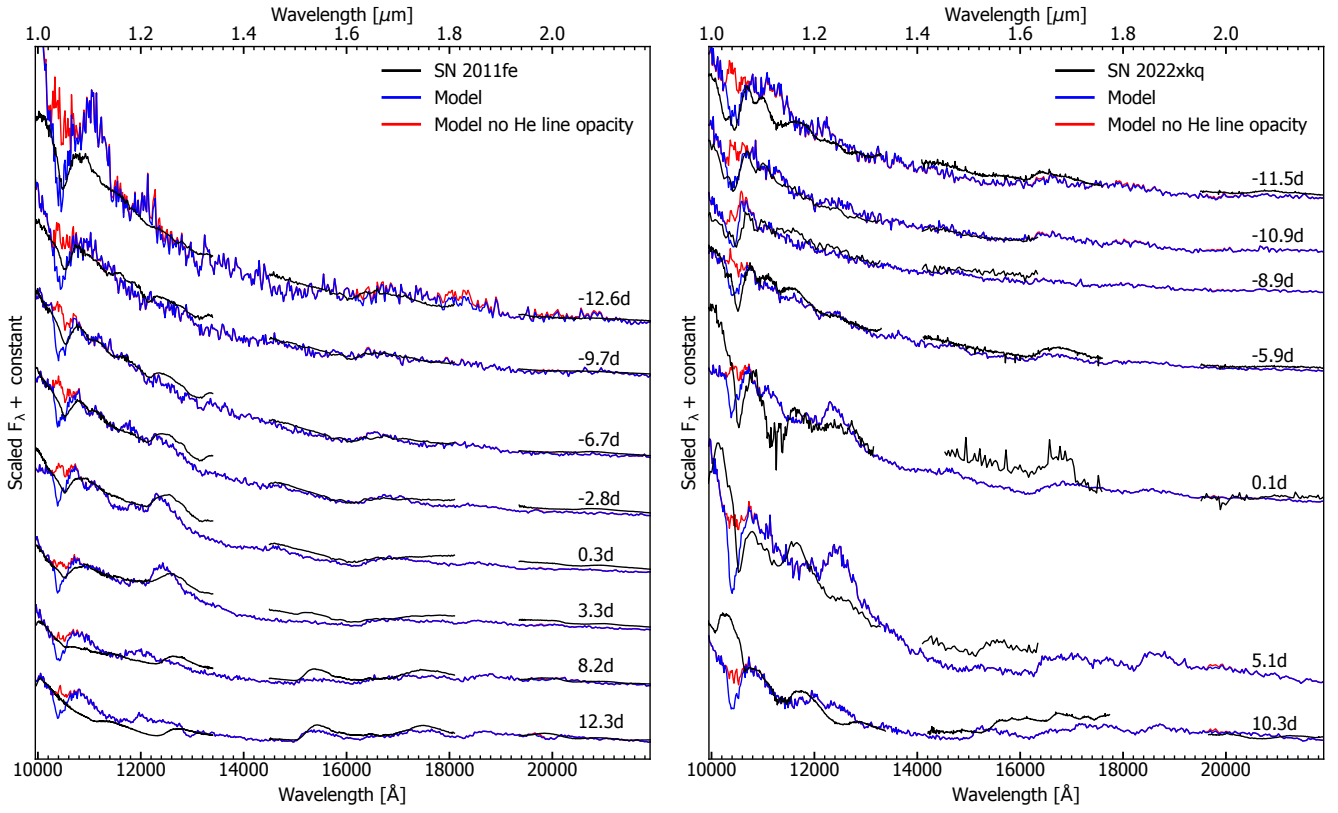


Figure A1. NIR spectroscopic evolution of our full model spectra and our model spectra in which the line opacity for He is not included, compared to SN 2011fe (Hsiao et al. 2013, left) and SN 2022xkq (Pearson et al. 2024, right). Times are relative to B -peak. Note, that for clarity the spectra of SN 2022xkq have been rebinned and the regions impacted by tellurics have been removed.